nature communications

Article

https://doi.org/10.1038/s41467-025-63563-3

Digital camouflage encompassing optical hyperspectra and thermal infrared-terahertz-microwave tri-bands

Received: 12 November 2024

Accepted: 21 August 2025

Rongxuan Zhu[1], Huanzheng Zhu[1], Bing Qin[1], Wenzhe Yao[1], Meng Zhao[1], Neng Yu[1], Zixian Su[2,3], Lijuan Xie[2,3], Hongbin Ma[4], Jiangtao Huangfu[4], Pintu Ghosh[1], Min Qiu[5] & Qiang Li[1] ✉

Modern reconnaissance technologies, including hyperspectral and multispectral intensity imaging across optical, thermal infrared, terahertz, and microwave bands, can detect the shape, material composition, and temperature of targets. Consequently, developing a camouflage technique that seamlessly integrates both spatial and spectral dimensions across all key atmospheric windows to outsmart advanced surveillance has yet to be effectively developed and remains a significant challenge. In this study, we propose a digital camouflage strategy that covers the optical (0.4-2.5 μm) hyperspectra and thermal infrared-terahertz-microwave (thermal IR (MWIR and LWIR)/THz/MW) tri-bands, encompassing over 80% of atmospheric windows. In the optical band, the hyperspectral digital camouflage can simulate various vegetational spectra as primary colors, with deviation rate less than 0.2 (can be regarded as the same type of plant). In the tri-bands, it also produces multilevel intensity digital camouflage within each band. The average structural similarity among multiple digital camouflage patterns is approximately 0.52, which is favorable for multispectral pattern-background matching. This work introduces a new paradigm in ultra-broadband electromagnetic wave manipulation by combining hyper/multi-spectra and spatial distribution, offering deeper insights into imaging, image processing, and information encryption technologies.

An effective camouflage technology should ideally mimic nature across all dimensions to efficiently conceal targets from advanced surveillance techniques. Approximately 63.52% of the Earth's land surface is covered by vegetation[1,2] (Fig. 1a), comprising 28.54% woodland, 23.31% grassland, 7.00% shrubland, and 4.67% tundra. In this complex background of organic substances and water, understanding how diverse materials contribute across different wavebands is essential. For example: (i) pigments such as carotenoids, chlorophyll, and lutein shape the spectral characteristics in the visible (VIS) band[3,4] (0.4–0.78 μm); (ii) plant cell structure and cellulose determine reflectance in the near-infrared (NIR) band[3–5] (0.78–1.4 μm); (iii) water influences spectral characteristics in the short-wave infrared (SWIR) band[4,6,7] (1.4–2.5 μm), contributes to high radiation properties in the thermal infrared (IR) bands[8,9] (3–5 μm and 8–14 μm), and affects responses in the terahertz (THz) band[10,11] (0.2–0.5 THz); and (iv) organic substances and water together exhibit complex responses in

---

[1]State Key Laboratory of Extreme Photonics and Instrumentation, College of Optical Science and Engineering, Zhejiang University, Hangzhou, China. [2]College of Biosystems Engineering and Food Science, Zhejiang University, Hangzhou, China. [3]The National Key Laboratory of Agricultural Equipment Technology, Beijing, China. [4]Laboratory of Applied Research on Electromagnetics, Zhejiang University, Hangzhou, China. [5]Key Laboratory of 3D Micro/Nano Fabrication and Characterization of Zhejiang Province, School of Engineering, Westlake University, Hangzhou, China. ✉e-mail: qiangli@zju.edu.cn

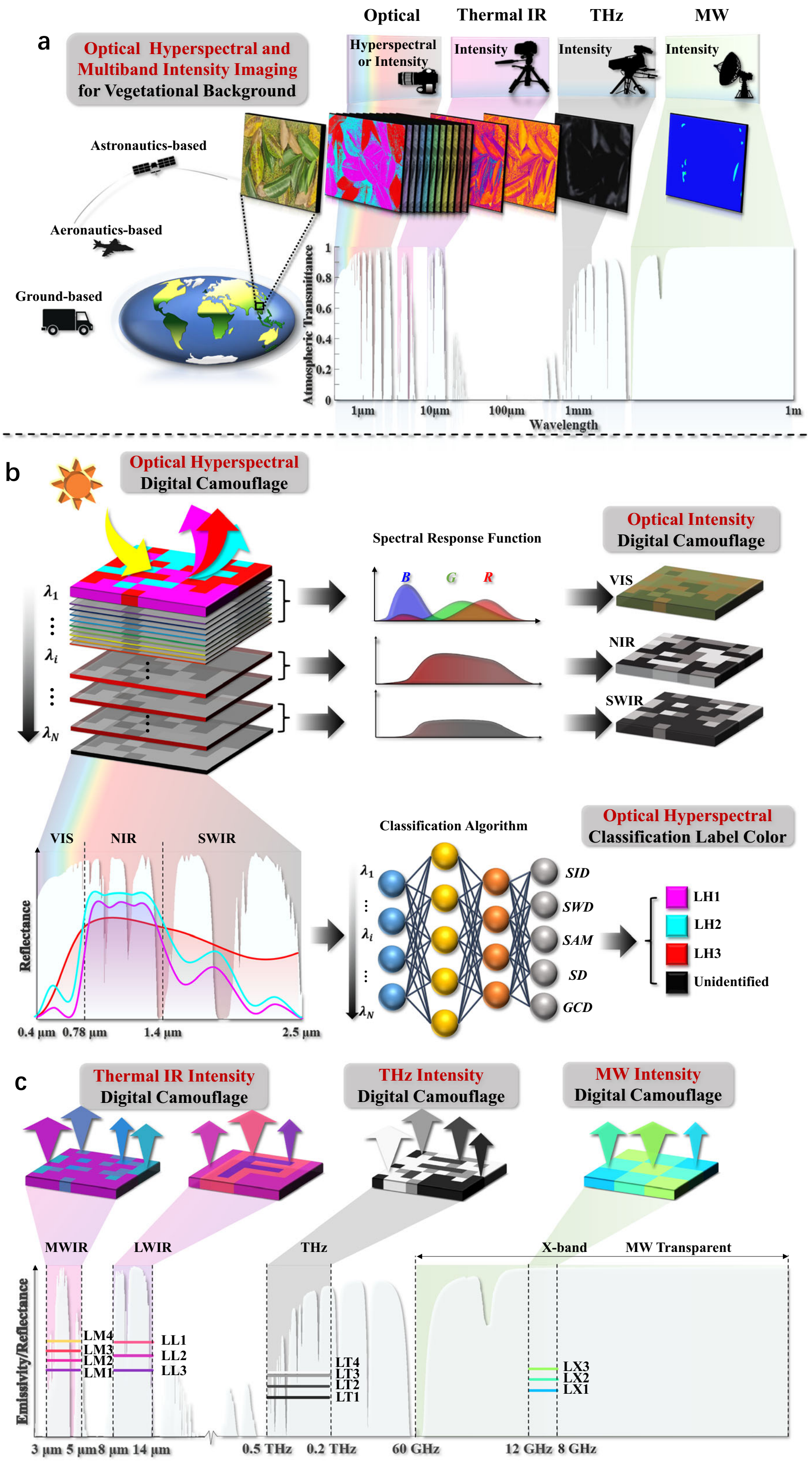

Fig. 1 | Principle of hyperspectral and ultra-broad multispectral intensity digital camouflage. **a** A visual representation of the threats confronting hidden targets in jungle environments, detected by various sensors operating across different wavelength bands and deployed from ground-based to space-based platforms. **b** Illustration of the optical hyperspectral digital camouflage and classification process (see definitions of relevant parameters in Supplementary Note 5). **c** Depiction of the multilevel intensity digital camouflage operating across the MWIR, LWIR, THz, and microwave MW bands.

the microwave (MW) band (1–60 GHz) with varied textures[12]. On one hand, camouflaging against this background, which contains organic materials and water, is particularly challenging. On the other hand, rapidly advancing imaging technologies, including high spatial and spectral resolution as well as ultra-broadband detection across all major atmospheric windows[13], are increasingly deployed in satellites, aircraft, and ground units, posing substantial threats to targets (Fig. 1a).

Three major aspects of imaging technologies that present significant challenges to achieving effective and robust camouflage are discussed below. First, ever-improving imaging technologies with greater spatial resolution (e.g., a camera with higher clarity, from 720 P to 1440 P) can detect the texture and shape of targets, necessitating digital camouflage technology to simulate natural patterns (e.g., the shape of the edges and contours of grass or prominent local features of leaves in the background). Digital camouflage achieves this by simulating background textures through spatial color mixing, outperforming traditional camouflage methods characterized by clear color boundaries and strong visual features. The design of digital camouflage patterns aligns with the characteristics of the human eye and visual psychology, effectively simulating background features such as color and texture, which counters high spatial resolution cameras and image processing algorithms[14–16]. Most digital camouflage primarily focuses on the VIS and infrared (IR) bands[17,18]. Second, hyperspectral imaging with high spectral resolution can detect the spectral fingerprints of targets[19,20], especially biochemical substances and water. Specifically, in the optical band, hyperspectral imaging excels in detecting vegetation due to the combination of high spectral resolution and spectral characteristics of plants, including the green peak, red edge, NIR plateau, and NIR/SWIR water absorption bands. This capability poses a significant threat to targets in vegetational backgrounds. This necessitates hyperspectral camouflage technology that mimics the spectral features of plants. Existing hyperspectral camouflage primarily employs two strategies: using pigments or microcapsules[6,21–25] with low thermal stability and multilayer structures[26,27]. Third, multispectral imaging that integrates optical, thermal IR, terahertz and microwave bands can detect the characteristics of targets in their corresponding bands[28] (Fig. 1a), compelling multispectral camouflage to cover all atmospheric windows. Multispectral camouflage counters the combination of multiple intensity imaging systems across various atmospheric ranges. In addition to the optical band, mid-wave infrared (MWIR, 3–5 μm) and long-wave infrared (LWIR, 8–14 μm) thermal imaging capture the radiation energy of targets, enhancing detection at night. The THz band is often utilized to monitor the water content of plants[10,11]. In the MW band, synthetic aperture radar (SAR) is employed for electromagnetic imaging[29,30]. Multispectral camouflage primarily uses nanostructures such as metasurfaces[31–46] and multilayer structures[47–58].

However, a robust camouflage technique that effectively integrates spatial features, hyperspectra, and multispectral intensity spanning all atmospheric windows has, so far, eluded previous camouflage efforts and presents significant challenges (see Supplementary Note 1). The two main challenges are as follows: (i) Combining spatial features with hyper/multi-spectra, which requires simulating various primary responses in the background, especially for hyperspectral applications. Additionally, variations in texture across the bands arise from different signal generation mechanisms: the target reflects the solar spectrum in the optical band, radiates heat from itself in the thermal IR band, and reflects electromagnetic signals in the THz/MW band. Therefore, the coupling among multiple camouflage patterns must be considered to ensure that the patterns for each band match the background. (ii) Achieving ultra-broadband coverage across all typical atmospheric windows. The wavelength spans approximately six orders of magnitude from VIS to MW (Fig. 1a), necessitating that the structural design of the device is compatible across the ultra-broadband range.

In this work, we propose a digital camouflage strategy encompassing VIS/NIR/SWIR hyperspectra and MWIR/LWIR/THz/MW multispectral intensity (Fig. 1b, c), primarily functioning in vegetational environments. This strategy achieves ultra-broadband digital camouflage that integrates optical hyperspectra and multispectral intensity, covering over 80% of typical atmospheric windows (see Supplementary Note 2).

Result

Strategy of digital camouflage

Digital camouflage fundamentally relies on the manipulation of color and pattern to counter detector arrays (e.g., complementary metal oxide semiconductor, charge-coupled device, and SAR arrays). The digital camouflage pattern can operate at optimal performance, with its colors and textures starting to blend into the background after reaching a certain distance from the detector (see Supplementary Note 3 for maximum object distance calculation and Supplementary Note 4 for lock-on range calculation). The method by which the digital camouflage device operates in the optical hyperspectral and thermal infrared-terahertz-microwave tri-bands is outlined as follows:

For optical hyperspectral digital camouflage, the primary colors are defined based on the main vegetational regions of interest (ROI) classification (the details of design method can be found in the Supplementary Note 5 and 6). This includes LH1 (fresh green vegetation), LH2 (fresh light-green vegetation), and LH3 (withered yellow vegetation) (Fig. 1b). Additionally, this study introduces a new theoretical framework and relevant parameter indicators for calculating spectral differences in digital camouflage (see Supplementary Note 5 and Supplementary data 1 and 2). As shown in Fig. 1b, a simple deep neural network (DNN) is trained to rapidly compute various hyperspectral image parameters and assist in classification algorithms (see Supplementary Note 5 and Supplementary data 1 and 2).

The optical hyperspectral digital camouflage pattern, composed of primary color pixels, replicates to the texture of vegetation in the hyperspectral image within the optical band (Fig. 1a). Therefore, optical hyperspectral camouflage pattern (spanning VIS, NIR, and SWIR bands in Fig. 1b) can be designed by integrating hyperspectral classification, background texture detection, pixelation, and patch templates (see Supplementary Note 6).

For thermal infrared-terahertz-microwave tri-bands digital camouflage, the primary color is referenced from Supplementary Note 7 and mapped to a color bar[17]. Here, the MWIR band is divided into 4-level (LM1-4), the LWIR band into 3-level (LL1-3), the THz band into 4-level (LT1-4), and the X-band into 3-level (LX1-3) (Fig. 1c).

The thermal infrared-terahertz-microwave camouflage patterns for the three bands are not fully optimized in this study. Due to the greater variability of signals in these bands (see Supplementary Note 7 for reference vegetational spectra and complex levels in real environment), obtaining accurate and effective background textures is challenging. To further improve and achieve optimal camouflage performance, the digital camouflage patterns should be independently designed according to the distinct signals in each band. This requires that the patterns for each band remain independent and decoupled from one another. For example, in Fig. 1c, the LWIR band pattern is designed in the shape of the letter "F" to preliminarily demonstrate the decoupling performance of the device. The coupling and decoupling methods for each band are discussed in detail in the Supplementary Note 5.

Structure of the digital camouflage device

The digital camouflage device consists of 64 (8 × 8) pixels which are configured into three different types: (i) fresh green vegetation simulation (GS), composed of ZnS (45 nm)/Ge (14 nm)/ZnS (130 nm)/Ti

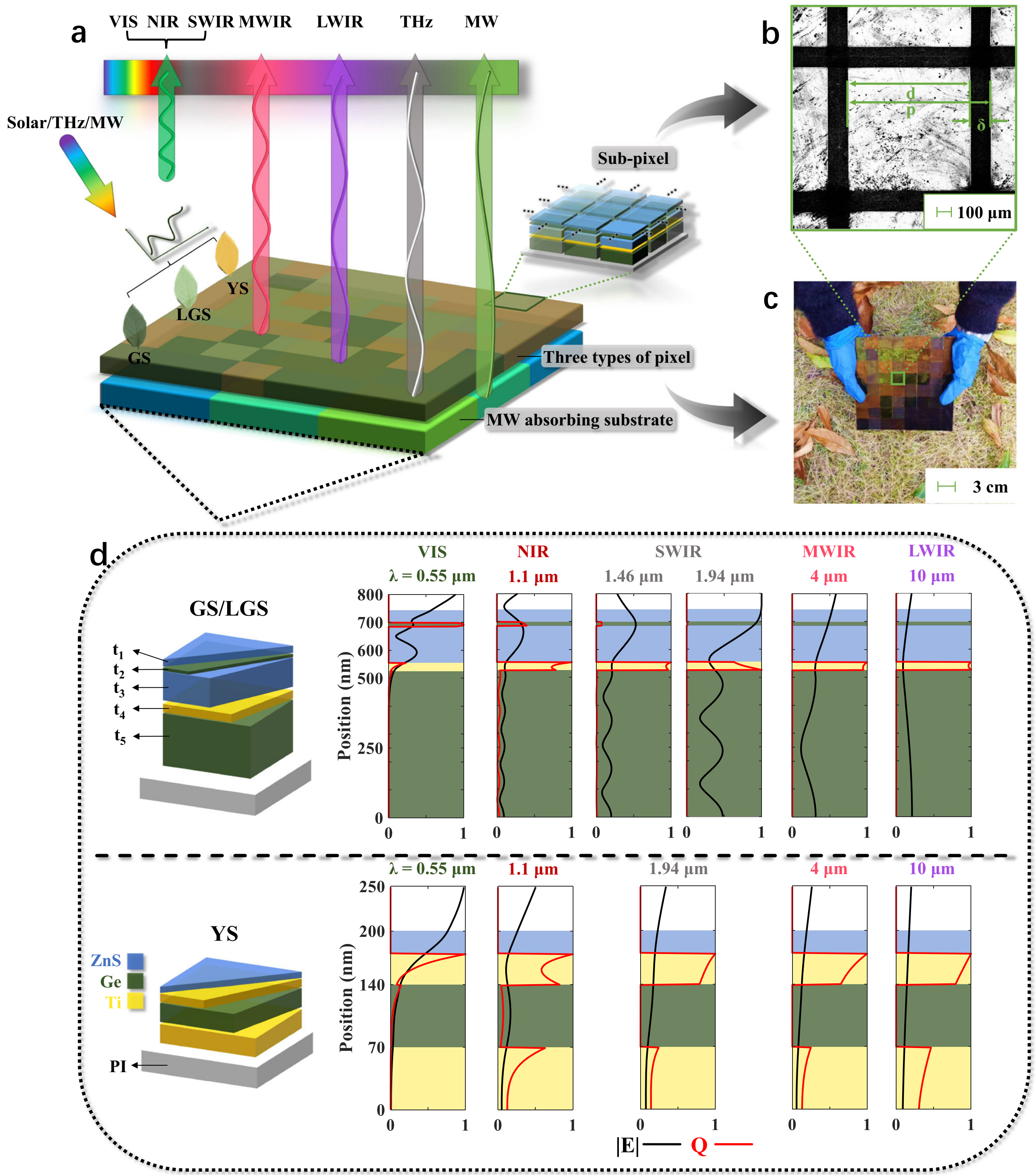

Fig. 2 | The pixel and multilayer structures. a Illustration of the various components and basic functions of the device. **b** Partial SEM overhead view of the device showing the effects of laser etching. **c** VIS image of the device captured using an ordinary camera. **d** The illustration depicts the multilayer structures of GS/LGS and YS, highlighting variations in layer thicknesses between GS and LGS, along with simulated electric field distribution (|E|) and resistive loss (Q) across wavelengths in the VIS, NIR, SWIR, MWIR, and LWIR bands for both GS and YS structures.

(30 nm)/Ge (524 nm) layers; (ii) fresh light-green vegetation simulation (LGS), made up of ZnS (37 nm)/Ge (20 nm)/ZnS (125 nm)/Ti (30 nm)/Ge (520 nm) layers (based on the same layer distribution. The thicknesses (t1, t2, etc.) in Fig. 2d were further optimized based on the plant spectra in Supplementary Note 7 using the method described in Supplementary Note 8; and (iii) withered yellow vegetation simulation (YS), consisting of ZnS (25 nm)/Ti (35 nm)/Ge (70 nm)/Ti (70 nm) layers (Fig. 2a-d). These three pixels are used to implement the primary colors of optical hyperspectral digital camouflage: LH1, LH2, and LH3, respectively.

Designing hyperspectral camouflage is challenging, as it requires the simultaneous optimization of numerous structural parameters and materials. To address this, a machine learning method based on the quadratic unconstrained binary optimization model is used to determine the optimal layer distribution[59–62] (see Supplementary Note 8 for details).

Each GS, LGS, and YS pixel contains 400 (20 × 20) rectangular sub-pixels (Fig. 2a). The dimension of each pixel is $20 \times 20\ \mathrm{mm}^2$ (Fig. 2b), which makes them indistinguishable to the human eye from a distance greater than 28 m (see detailed maximum object distance calculation in Supplementary Note 3). The period of the sub-pixels, denoted as p, is 1 mm (Fig. 2a, b). The sub-pixels have three variants with linewidths, δ, measuring 10 µm, 77 µm, and 150 µm, corresponding to areal duty cycles of 98.01%, 85.19%, and 72.25%, respectively (Fig. 2a, b). All these structures are deposited on a 125 µm thick polyimide (PI) film, which is placed on top of an MW absorbing substrate (Fig. 2a).

Spectral performance

To illustrate the mechanisms of optical hyperspectral camouflage, the modal field analysis of GS/LGS and YS is performed (Fig. 2d), revealing that the optical spectra are generated by a combination of antireflection, Fabry-Pérot (F-P) resonance, and intrinsic properties of materials in the multilayer structures (Figs. 2d and 3a). For GS/LGS, they have similar structures and exhibit comparable spectral performance (a detailed physical analysis is shown in Supplementary Note 9): (i) The green peak is precisely aligned at 0.55 µm, formed by the F-P resonance and antireflection effects of the four-layer ZnS/Ge/ZnS/Ti structure. (ii) The red edge and NIR plateau (~1.1 µm) meet military specifications[63], which is formed by the high reflectance of the Ti layer and the decreasing intrinsic loss of Ge. (iii) The four water absorption bands in the NIR/SWIR exhibit increasing absorption from shortwave to longwave, resulting from the resonances of all layers. For YS: (i) the green edge (~0.55 µm) and the NIR plateau (~1.1 µm) effectively simulate withered yellow leaves; (ii) the SWIR water absorption band at 1.94 µm is used to simulate weak water absorption.

Optical hyperspectral digital camouflage can be generated after classifying the spectra of GS, LGS, and YS as LH1, LH2, and LH3, respectively. The digital camouflage exhibits the effect of spatial color mixing (spectral mixing) when observed from a distance. Following the spectral mixing of GS, LGS, and YS, the average optical spectrum meets military specifications (black solid line in Fig. 3a, the spectra of common plants can be found in Supplementary Note 10).

The MWIR/LWIR/THz multilevel spectra and MW transparency are generated by sub-pixels (Figs. 2a, b, and 3b-d). In the MWIR and LWIR bands, the device shows 4-level spectra (LM1-4 in Figs. 3b) and 3-level spectra (LL1-3 in Fig. 3b), respectively. These levels are primarily formed due to the duty cycle of the sub-pixels (see Supplementary Note 11 for thermal infrared decoupled method). The LM4 spectrum is created by the total structural resonance between GS and LGS pixels, which is evident from the electric field distribution and resistive loss plots at approximately 4 µm wavelength (Fig. 2d). For the thermal IR dual-band digital camouflage pattern, the emissivity difference between each level exceeds 0.08. In the THz band, the 4-level spectra (LT1-4 in Fig. 3c) are produced by the combination of the sub-pixels and PI substrate, simulating the reflectance of plants with varying water content (see Supplementary Note 7 and 9). For the THz digital camouflage pattern, the reflectance difference between each level is greater than 1 dB.

The X-band digital camouflage pattern is formed by the MW absorbing substrate (Fig. 2a), which is completely decoupled from other bands (see Supplementary Note 5 and 12). In the X-band, the 3-level reflectance spectra (LX1-3 in Fig. 3d) are generated by various types of MW absorbing materials (see Supplementary Note 12). For the X-band digital camouflage pattern, the reflectance difference between each level exceeds 0.6 dB, and the average reflectance is lower than −7 dB, demonstrating radar camouflage capabilities.

The average structure similarity index measure (*SSIM*) among optical hyperspectral pattern and MWIR/LWIR/THz/MW pattern is 0.52 (Fig. 1c). The low average *SSIM* indicates the low coupling and high design freedom of this digital camouflage strategy, allowing it to match background textures across multiple bands.

Optical hyperspectral digital camouflage

The performance of hyperspectral digital camouflage is verified in a simulated jungle scenario by two hyperspectral cameras operating in wavelength ranges 0.4–1.0 µm and 1.0–2.5 µm (Fig. 4a, NIR/SWIR images of the device are shown in Supplementary Note 13). The references, which consist of green, light green, and yellow colors, include dyed fabrics and painted aluminum plates. The two types of references are used to represent camouflage uniforms/paint commonly used in equipment. In the background, the green leaf, light-green grass, and withered yellow leaf serve as the ROIs in the spectral information divergence (SID) classification (Fig. 4b, c). Furthermore, for spectral analysis and comparison, Fig. 4d presents the spectra of the device, references, and plants, with corresponding VIS colors (green, light-green, and yellow marked points in Fig. 4a).

In the band of 0.4–1.0 µm, the device displays a hyperspectral digital camouflage pattern with three labeled colors, LH1-3 (Fig. 4b). For GS, the green peak is lower than 10%, and the red edge meets the specifications, forming a green VIS color. The NIR plateau of GS is around 60%, which is consistent with the range of vegetation. For LGS, the green peak is slightly higher (~15%), and the red edge also meets the specifications, forming a light-green VIS color. The NIR plateau for LGS is slightly elevated to around 65%. For YS, the spectrum lacks the green peak feature and rises directly from the green edge to the NIR plateau of about 50%, forming a yellow VIS color. In contrast, for fabric and paint references, the mismatch of spectral features leads to local misidentified or unidentified regions, thus compromising the camouflage (Fig. 4b). Their green peak cannot align with 0.55 µm, and the red edge does not meet the detection specifications, showing a metamerism effect. Additionally, the NIR plateau of the fabric and paint references is excessively high.

In the band of 1.0–2.5 µm, which is primarily for water monitoring, the device exhibits a variety of water contents and retains texture features (Fig. 4c). Although the device has few misidentified regions due to ambient light, it can still maintain camouflage. For GS and LGS, the 1.46 µm and 1.94 µm dips clearly exhibit water absorption features, and the spectral trend aligns with the specifications (Fig. 4d). The YS shows almost no water absorption while the spectrum still aligns with the specifications. In contrast, for fabric and paint references, their spectra lack water absorption bands and contain many noise peaks due to fabric fibers or paint solvents, failing to meet the specifications. As a result, there is a complete loss of texture features, which directly exposes the underlying object (Fig. 4c).

To summarize the performance in the experimental scenario, the deviation rate between the digital camouflage device and the background vegetation is less than 0.2 (can be regarded as the same type of plant, see detailed discussion in Supplementary Note 5). Specifically, for more detailed spectral metrics calculations, see Supplementary Note 5 and 13. The long distance optical hyperspectral digital camouflage results can be found in Supplementary Note 6.

Thermal IR-THz-MW intensity digital camouflage

The thermal IR-THz-MW tri-bands experiments are performed to demonstrate the multispectral intensity digital camouflage performance in a simulated grassy background (Figs. 5 and 6). The device shows 4-level and 3-level thermal digital camouflage patterns at 100 °C through MWIR (Fig. 5a, b) and LWIR (Fig. 5c, d) imaging, respectively. In contrast, the fabric and paint references exhibit the black body radiation property with no patterns. In the MWIR and LWIR bands, the device reduces the radiation temperature by about 40 °C compared to the fabric and paint, and the radiation temperature difference between each level is about 2 °C. At longer distances (10 m, approximately equal to the maximum object distance; see Supplementary Note 3 for the calculation of the maximum object distance and Supplementary Note 14 for detailed thermal IR experiments), the digital camouflage device exhibits a blending performance with the background,

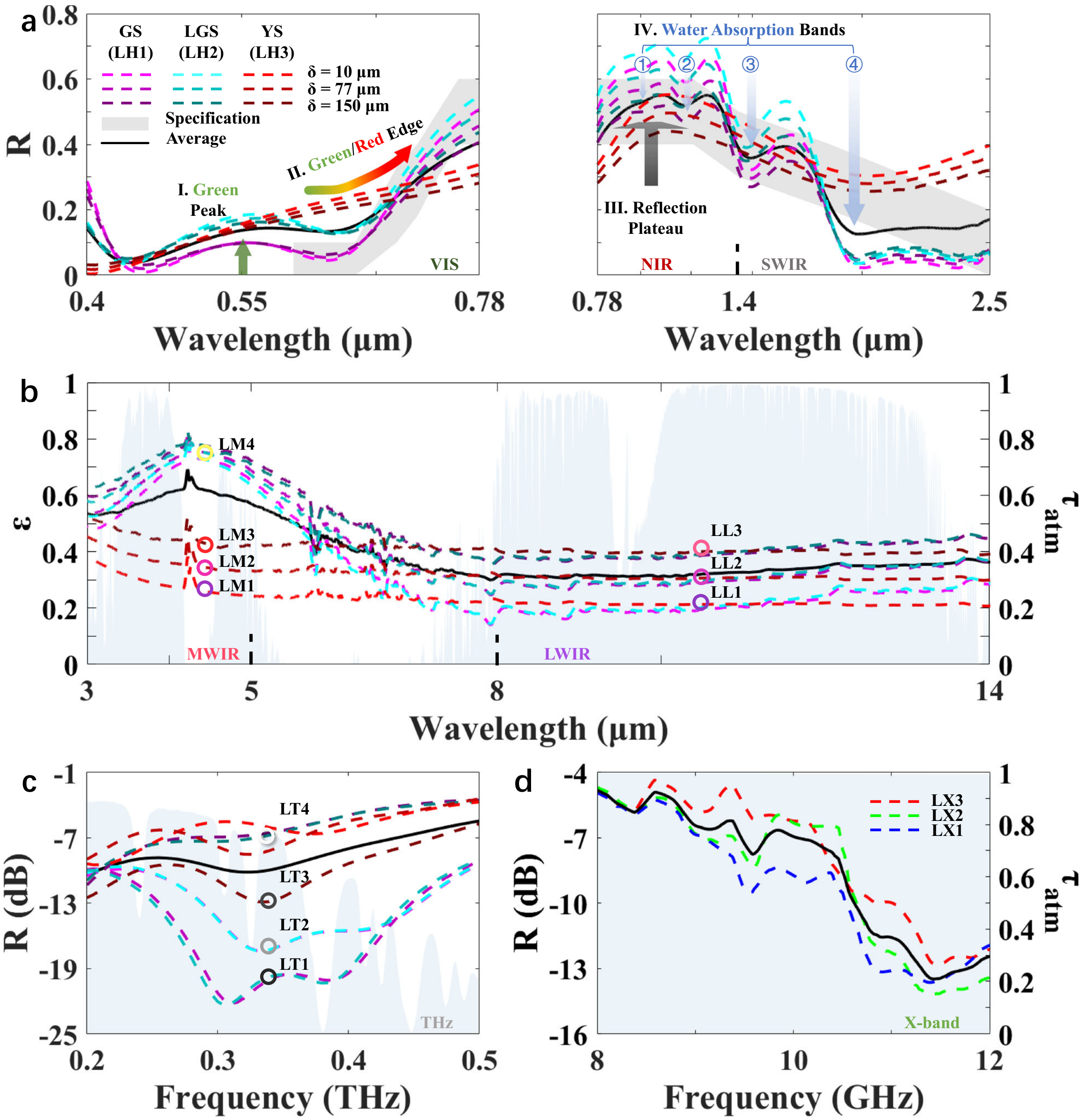

Fig. 3 | Multilevel reflectance, transmittance, and emissivity spectra of pixels. **a** Experimental reflectance spectra of the three structures (GS, LGS, and YS) in the VIS, NIR, and SWIR bands. **b** Experimental emissivity spectra of the three structures in the MWIR and LWIR bands, categorized into four levels (LM1-4) for the MWIR band and three levels (LL1-3) for the LWIR band. **c** Experimental reflectance spectra of the three structures in the THz band, showing four levels (LT1-4). **d** Experimental reflectance spectra of the whole device (including the structures and the MW-absorbing substrate) and average transmittance spectra of the microwave-absorbing substrate. The inset shows the zoomed-in X-band spectra and the corresponding three levels (LX1-3).

effectively camouflaging a 100 °C target to appear close to ambient temperature (Fig. 5b, d), whereas the fabric and paint references remain exposed against it. The MWIR pattern presents an additional level due to the emissivity difference of withered vegetation (see Supplementary Note 7). The LWIR pattern of the letter “F” demonstrates the ability to design independent patterns across multiple bands.

In the THz and MW bands, a steel plate is placed under the samples as a target. The device demonstrates 4-level and 3-level digital camouflage patterns through THz and X-band imaging, respectively. In contrast, the fabric reference appears almost transparent. The paint reference also exposes the target due to the aluminum plate substrate. In the THz band, the grassy background displays differences in plant water content, and the maximum background reflectance exceeds 6 dB (Fig. 6a, b). The maximum intensity difference of the digital camouflage device exceeds 7 dB, demonstrating the simulation of varying water content. At longer distances (0.4 m, approximately equal to the maximum object distance), the digital camouflage device also exhibits a blending performance with the background (Fig. 6b, d, due to experimental limitations that prevent long-distance imaging, simulation images are provided instead). The THz pattern presents an additional level due to the transmission of vegetation spectra (see Supplementary Note 7). In the MW band, under X-band SAR, the grassy background is also non-uniform due to biochemical substances. The

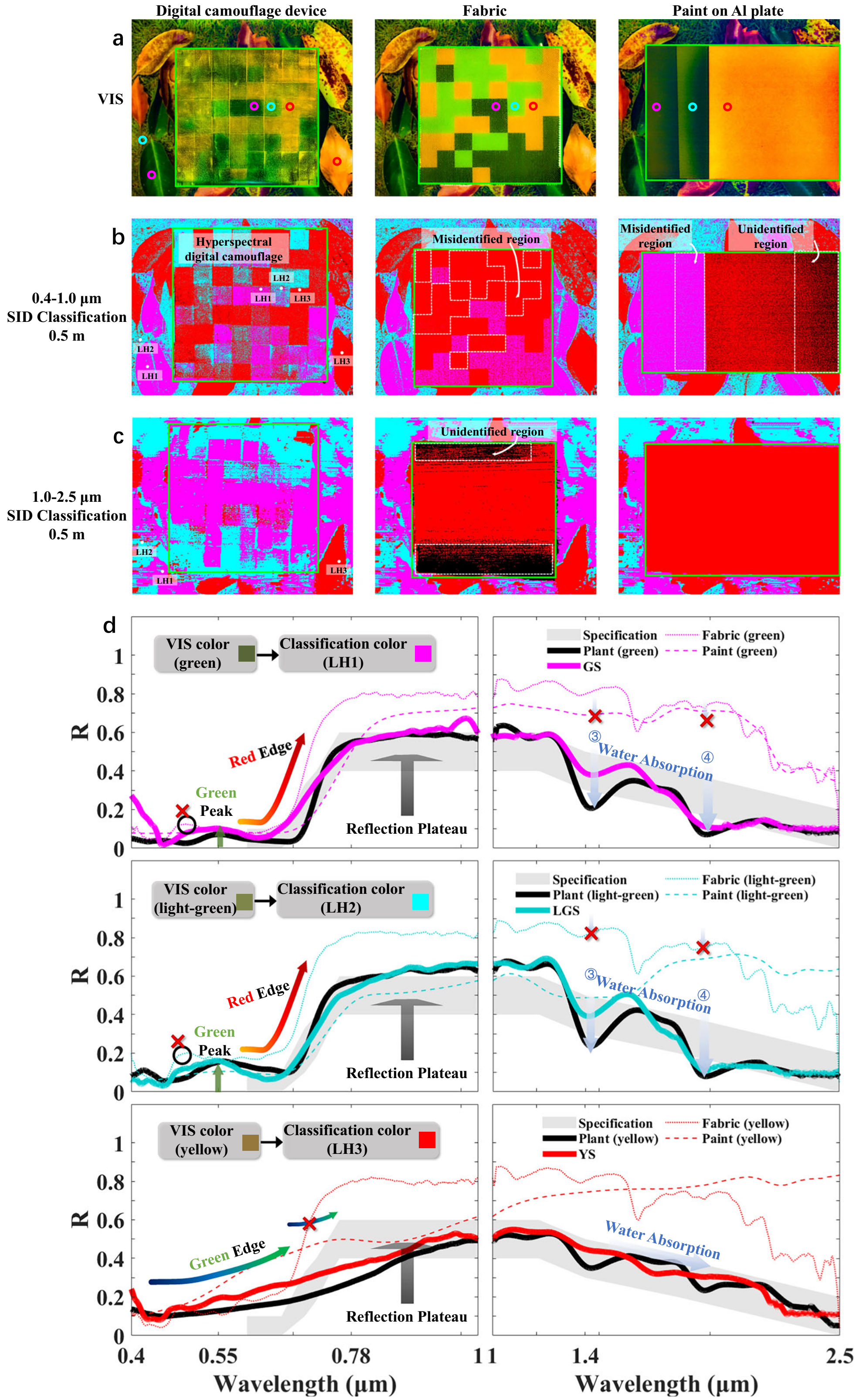

Fig. 4 | **Hyperspectral digital camouflage. a** A simulated jungle scenario created in an experimental black box, displaying VIS images of the device, fabric reference, and paint reference. **b** SID classification images in the 0.4–1.0 µm range, reflecting basic spectral features in the VIS/NIR spectrum. **c**. SID classification images in the 1.0–2.5 µm range, highlighting water features. **d** Spectral diagrams illustrating three types of vegetation and various camouflage samples.

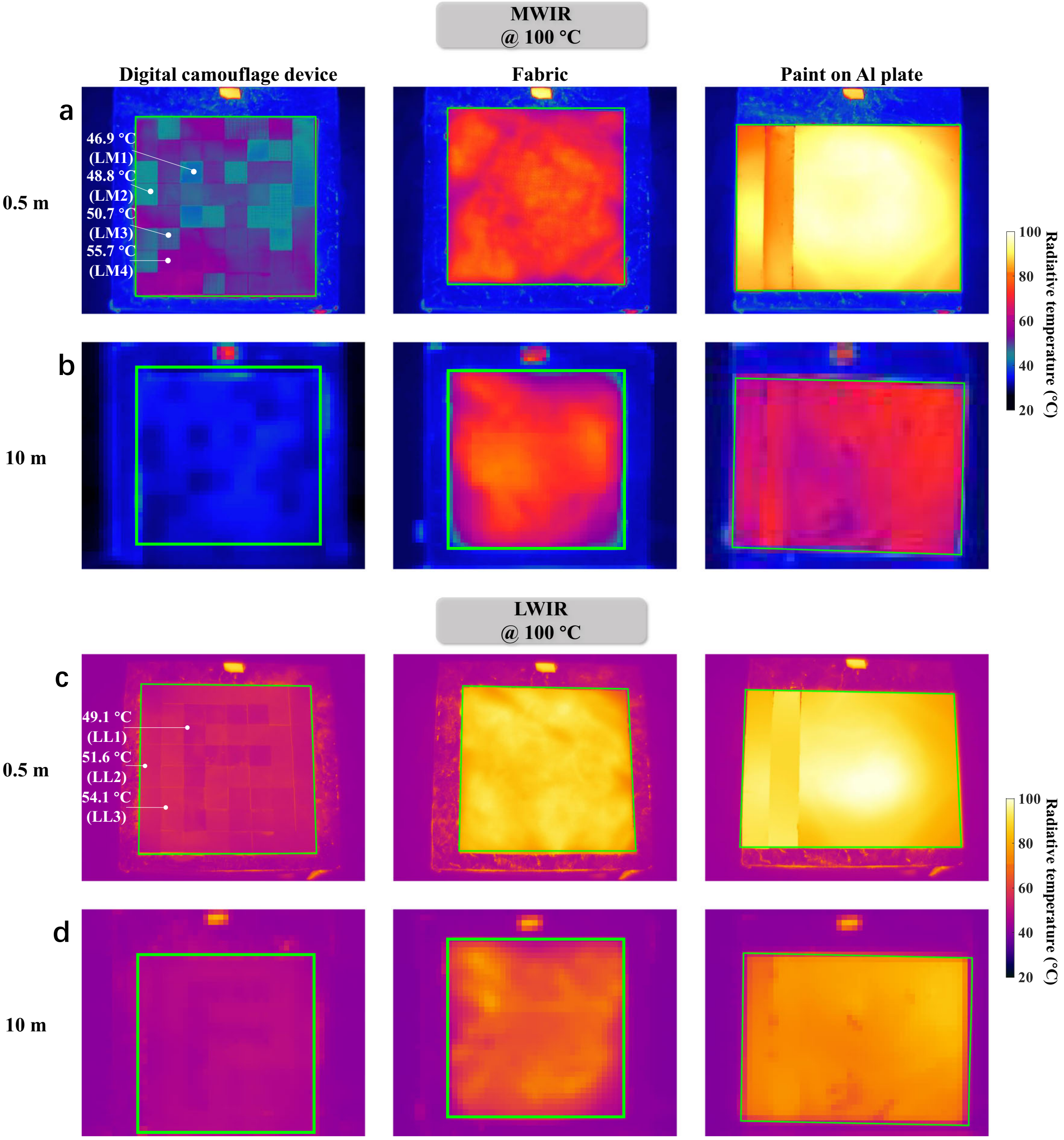

Fig. 5 | MWIR/LWIR digital camouflage. A thermal infrared comparison of the digital camouflage performance between the device and two references (fabric and paint on Al plate). MWIR images captured at distances of (**a**). 0.5 m and **b** 10 m, LWIR images captured at distances of (**c**). 0.5 m and **d** 10 m. For the MWIR and LWIR bands, the samples are placed on a hot plate at 100 °C. The corresponding optical images of the device and the references are shown in Fig. 4a.

intensity difference of the digital camouflage is greater than 0.6 dB, and the average reflectance is less than -7 dB, demonstrating MW absorbing performance (Fig. 6c, d).

Additionally, it should be noted that in Fig. 5a and Fig. 6a, camouflage patterns do not blend well with the background at a short distance. As mentioned earlier, passive camouflage cannot perfectly adapt to all background environments (factors such as temperature and moisture can affect the background's reflectance or emissivity response). The patterns still maintain camouflage effectiveness, although they require greater distance than perfect pattern (Figs. 5b and 6b), to escape detection by the sensor (see Supplementary Note 3 for maximum object distance calculation, Supplementary Note 4 for lock-on range calculation). Furthermore, there are potential improvements, such as decoupling and independently designing patterns for the thermal IR and THz bands (see Supplementary Note 10 and 11), which would allow them to perfectly align with the background.

Discussion

A digital camouflage strategy that incorporates optical hyperspectra and thermal IR-THz-MW tri-bands based on multilayer structures is developed. Firstly, this work advances (i) digital camouflage from mere color or intensity to hyperspectral applications and (ii) improves previous camouflage methods by extending coverage to over 80% of typical atmospheric windows (see Supplementary Note 2). Thereby, the proposed digital camouflage strategy features capabilities and performance metrics that either exceed or match the state of the art in passive digital camouflage and hyper/multi-spectral camouflage technologies (see Supplementary Note 1). Secondly, the optical hyperspectral pattern of the device can adapt to various backgrounds and seasonal variations (e.g., maple forests, sapium sebiferum forests, and metasequoia glyptostroboides forests) by adjusting the proportions of different types of digital pixels (see Supplementary Note 7 and 9). Thirdly, the coupling among the device's multispectral patterns can be eliminated, allowing each band's pattern to be designed more independently. In this work, a

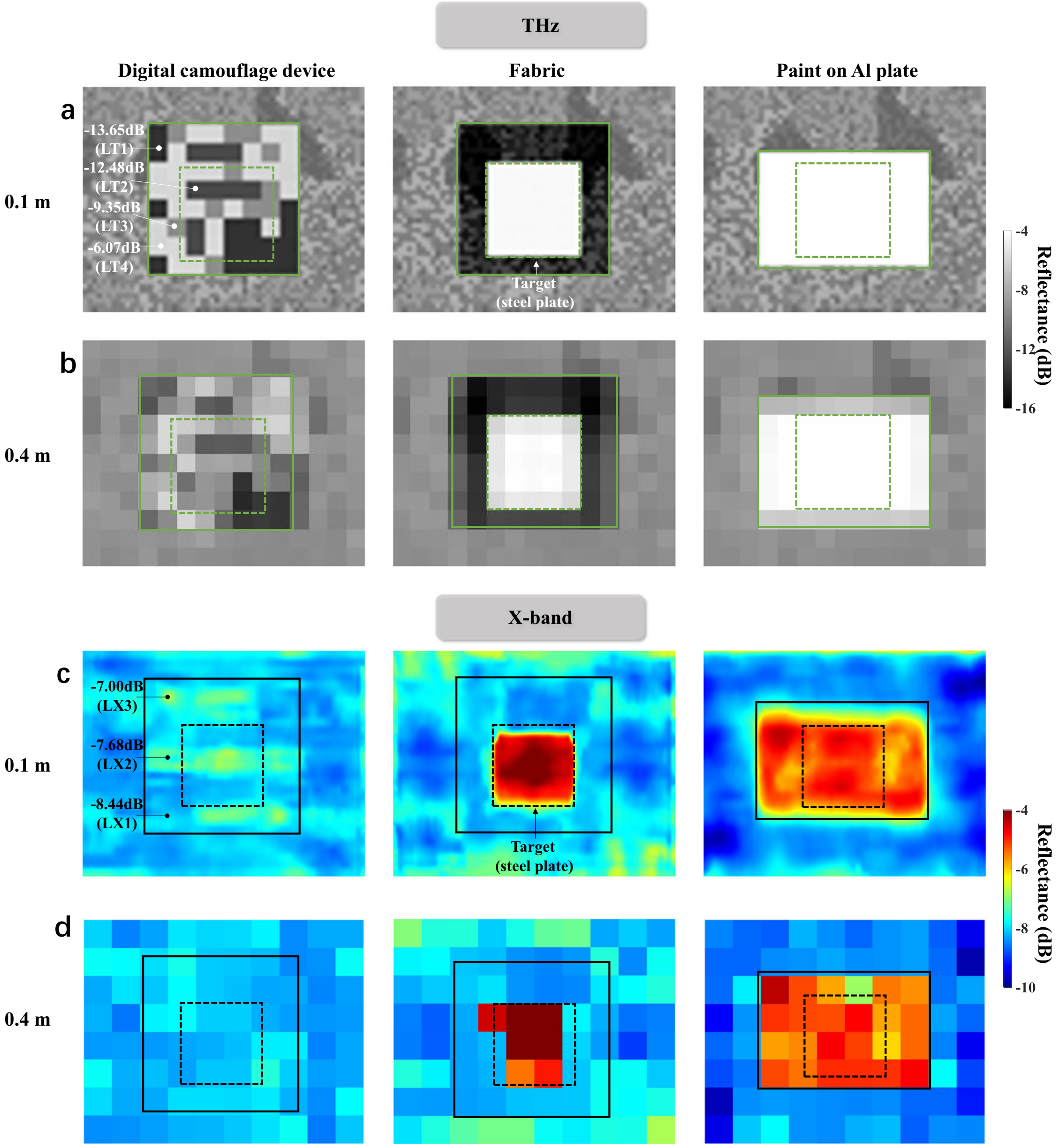

Fig. 6 | THz/X-band digital camouflage. A THz/MW comparison of the digital camouflage performance between the device and two references (fabric and paint on Al plate). A steel plate is placed under the samples as a target. **a** THz experimental images captured at distances of 0.1 m, **b** THz simulation images captured at distances of 0.4 m, **c** X-band experimental images captured at distances of 0.1 m, **d** X-band simulation images captured at distances of 0.4 m. The THz digital camouflage mimics water characteristics. The X-band digital camouflage is presented under SAR imaging, along with MW absorption camouflage. The corresponding optical images of the device and the references are shown in Fig. 4a.

strategy is employed to further decouple the digital camouflage: in the thermal IR band, the radiation energy patterns are formed by controlling the average emissivity through sub-pixels with different duty cycles, which is equivalent to the emissivity pattern. Another temperature pattern can be generated by incorporating an insulating layer that utilizes materials with different thermal conductivities (see Supplementary Note 10). The radiation energy patterns are modulated by varying the emissivity and the temperature without affecting the patterns of other bands. In the case of complete decoupling with m levels of patterns for each of n spectral bands, a total of m^n structural designs would be required, which poses a significant challenge for structural optimization. Additionally, the strategy has the potential for large-scale manufacturability and straightforward integration, making it applicable for individual combat technology (see Supplementary Note 14) for the following reasons: (i) optical hyperspectral and thermal IR functions are achieved through a simple flexible multilayer structure; (ii) THz function is realized by laser-etched sub-pixels; and (iii) MW functions are achieved using commercially available flexible absorbing materials produced on a large scale, and are compatible with communication (e.g., 2.4 GHz). Lastly, the device increases the upper temperature limit for hyperspectral camouflage operations and facilitates targets with electrical components or engines through its thermal stability, with the multilayer structure capable of withstanding high temperatures up to 350 °C (see Supplementary Note 15). Ultimately, this research opens opportunities for the simultaneous manipulation of hyperspectral or multispectral electromagnetic waves and spatial features, thereby advancing hyper/multi-spectral imaging, image processing, and information encryption technologies[36,64–70].

Methods

Simulation

The simulation of the absorptivity/emissivity spectra are accomplished by leveraging the transfer matrix method and COMSOL Multiphysics. Additionally, COMSOL Multiphysics is employed to simulate the distribution of the electric field intensity.

Fabrication

The multilayer structures are prepared by electron beam evaporation (EBE) with deposition rates of 4 Å/s (ZnS), 4 Å/s (Ge), and 1 Å/s (Ti). The heating operation commences once the vacuum degree reaches 2×10^{-6} Torr. Following the creation fabrication of the multilayer structure, laser etching is processed performed by Hangzhou Silver-Lake Laser Technology Co., Ltd. The MW absorbing materials are purchased from Shenzhen Schutt Technology Co., Ltd.

Optical characterization

The optical reflection spectra are measured using a universal measurement spectrophotometer (Cary7000, Agilent) equipped with a universal measurement accessory (UMA). The incident angle of the light source onto the samples is about 6°. The optical hyperspectral images in the range of 0.4–1.0 μm are captured using a hyperspectral camera (GaiaField-ProR10, Dualix Spectral Imaging) with a spectral resolution of 2.5 nm. The optical hyperspectral images in the range of 1.0–2.5 μm are captured using a hyperspectral camera (GaiaField-ProR25-HSW, Dualix Spectral Imaging) with a spectral resolution of 10 nm.

Thermal IR characterization

The thermal IR spectra spanning from 2.5 to 14 μm is measured by exploiting an FTIR spectrometer (Vertex 70, Brucker). A Jenoptik camera is employed to measure the radiative temperature in the LWIR band. A Telops camera is used to measure the radiative temperature in the MWIR band. The absolute temperature is measured using thermocouples (5TC-TT-K-30-36, Omega).

THz characterization

The THz spectra are measured by exploiting a compact and multi-purpose terahertz spectroscopic (TAS7500SP, Advantest). The THz images are captured using a spectrometer (TAS7500SP) with multi-point scanning calibration. The field scanning area is 360×240 mm^2 (the invalid regions are cut off) with a spatial resolution of 5×5 mm^2.

MW characterization

The MW reflection/transmission spectra are measured using the arc method and free-space method in Wuzhen Laboratory, respectively. In the X-band imaging, an X-band standard horn antenna was used to generate the desired incident waves. A short monopole (a small loop antenna) was used as the field probe to detect the electric fields (the magnetic fields) in the space, for TE (TM) polarization. The probes' movement is driven by a mechanical scanner, and the point-to-point field scanning in the xz-plane is realized. The horn antenna was placed around 50 cm away from the sample. The field scanning area is 560×240 mm^2 (the invalid regions are cut off) with a spatial resolution of 8×8 mm^2.

Data availability

The optical, thermal infrared, terahertz, and microwave spectra data generated in this study are provided in the Supplementary data 3.

References

1. NASA Astrobiology Institute. *Atmospheric Seasons Could Signal Life on Exoplanets*, <https://astrobiology.nasa.gov/nai/articles/2018/5/24/atmospheric-seasons-could-signal-life-on-exoplanets/> (2018).
2. National Catalogue Service for Geographic Information. *Geographic statistics based on GlobeLand 30*, <https://www.webmap.cn> (2010).
3. Lv, X. et al. Structure and near-infrared spectral properties of mesoporous silica for hyperspectral camouflage materials. *Infrared Phys. Technol.* **129**, 104558 (2023).
4. Woolley, J. T. Reflectance and transmittance of light by leaves. *Plant Physiol.* **47**, 656 (1971).
5. Liu, Z. et al. Design of biomimetic camouflage materials based on angiosperm leaf organs. *Sci. China Ser. E Technol. Sci.* **51**, 1902–1910 (2008).
6. Huang, Z. et al. A color-changing biomimetic material closely resembling the spectral characteristics of vegetation foliage. *Small* **20**, 2303966 (2024).
7. Sims D A, G. J. A. Relationships between leaf pigment content and spectral reflectance across a wide range of species, leaf structures and developmental stages. *Remote Sens. Environ.* **81**, 337–354 (2002).
8. Coutts, A. M. et al. Thermal infrared remote sensing of urban heat: hotspots, vegetation, and an assessment of techniques for use in urban planning. *Remote Sens. Environ.* **186**, 637–651 (2016).
9. Guillevic, P. et al. Thermal infrared radiative transfer within three-dimensional vegetation covers. *J. Geophys. Res. Atmos.* **108**, D8 (2003).
10. Gente, R. et al. Monitoring leaf water content with THz and sub-THz waves. *Plant Methods* **11**, 15 (2015).
11. Jördens, C. et al. Investigation of the water absorption in polyamide and wood plastic composite by terahertz time-domain spectroscopy. *Polym. Test.* **29**, 209–215 (2010).
12. Shi, J. et al. Microwave vegetation indices for short vegetation covers from satellite passive microwave sensor AMSR-E. *Remote Sens. Environ.* **112**, 4285–4300 (2008).
13. MODTRAN. *MODTRAN Infrared Light in the Atmosphere*, <https://climatemodels.uchicago.edu/modtran/> (2015).
14. Xue, F. et al. Design of digital camouflage by recursive overlapping of pattern templates. *Neurocomputing* **172**, 262–270 (2016).
15. Jia, Q. et al. Design and evaluation of digital camouflage pattern by spot combination. *Multimed. Tools Appl.* **79**, 22047–22064 (2020).
16. Xiao, H. D. et al. Fast self-adaptive digital camouflage design method based on deep learning. *Appl. Sci.* **10**, 5284 (2020).
17. Xu, C. et al. The relationship between spatial color mixing with color and radiation similarity in digital camouflage study. *Infrared Phys. Technol.* **130**, 104593 (2023).
18. Cui, Y. A. et al. Visible transparent wideband microwave meta-absorber with designable digital infrared camouflage. *Adv. Optical Mater.* **12**, 2301712 (2023).
19. Schimleck, L. et al. Review of near-infrared hyperspectral imaging applications related to wood and wood products. *Appl. Spectrosc. Rev.* **58**, 585–609 (2023).
20. Hu, X. et al. Hyperspectral anomaly detection using deep learning: a review. *Remote Sens.* **14**, 1973 (2022).
21. Xie, D. et al. A hyperspectral camouflage colorant inspired by natural leaves. *Adv. Mater.* **35**, e2302973 (2023).
22. Lu, Q. X. et al. Green plant leaf-inspired smart camouflage fabrics for visible light and near-infrared stealth. *J. Bionic Eng.* **19**, 788–798 (2022).
23. Lu, H. et al. Hyperspectral camouflage coating using Palygorskite to simulate water absorption of healthy green leaves. *Mater. Sci. Semiconductor Process.* **156**, 107293 (2023).
24. Gao, Y. et al. A camouflage coating with similar solar spectrum reflectance to leaves based on polymeric inorganic composite. *Mater. Res. Express* **8**, 066404 (2021).
25. Yang, P. et al. Hyperspectral and weather resistant biomimetic leaf enabled by interlayer confinement. *Adv. Funct. Mater.* **34**, 2405908 (2024).

26. Deng, Z. et al. Biomimetic multilayer film simulating solar spectrum reflection characteristics of natural vegetations for optical camouflage. *Opt. Express* **31**, 37082–37093 (2023).
27. Ding, C. L. et al. Design and fabrication of a multiband compatible stealth film in green circumstance. *Optical Mater.* **131**, 112622 (2022).
28. Chandra, S. et al. Adaptive multispectral infrared camouflage. *ACS Photonics* **5**, 4513–4519 (2018).
29. Huang, C. et al. Graphene-driven metadevice for active microwave camouflage with high-efficiency transmission window. *Small Methods* **5**, e2000918 (2021).
30. Sun, Y. et al. Electromagnetic metasurface with object information and position illusion in radar vision at microwave frequencies. *Adv. Optical Mater.* **11**, 2300318 (2023).
31. Zhang, Z. et al. Diffusion metamaterials. *Nat. Rev. Phys.* **5**, 218–235 (2023).
32. Ergoktas, M. S. et al. Localized thermal emission from topological interfaces. *Science* **384**, 1122–1126 (2024).
33. Cai, T. et al. Experimental realization of a superdispersion-enabled ultrabroadband terahertz cloak. *Adv. Mater.* **34**, e2205053 (2022).
34. Liu, X. et al. A bioinspired bilevel metamaterial for multispectral manipulation toward visible, multi-wavelength detection lasers and mid-infrared selective radiation. *Adv. Mater.* **35**, e2302844 (2023).
35. Wang, J. et al. Multilevel information encryption mediated by reconfigurable thermal emission in smart bilayer material. *Laser Photonics Rev.* **18**, 2301106 (2024).
36. Liang, L. et al. MXene-enabled pneumatic multiscale shape morphing for adaptive, programmable and multimodal radar-infrared compatible camouflage. *Adv. Mater.* **36**, e2313939 (2024).
37. Kim, T. et al. Hierarchical metamaterials for multispectral camouflage of infrared and microwaves. *Adv. Funct. Mater.* **29**, 1807319 (2019).
38. Lee, G. et al. Ultrathin metal film on graphene for percolation-threshold-limited thermal emissivity control. *Adv. Mater.* **35**, e2301227 (2023).
39. Liu, X. et al. Thermochromic infrared metamaterials. *Adv. Mater.* **28**, 871–875 (2016).
40. Wu, R. et al. Spectrally engineered textile for radiative cooling against urban heat islands. *Science* **384**, 1203–1212 (2024).
41. Xu, C. et al. Adaptive infrared-reflecting systems inspired by cephalopods. *Science* **359**, 1495–1500 (2018).
42. Li, Z. et al. Brochosome-inspired binary metastructures for pixel-by-pixel thermal signature control. *Sci. Adv.* **10**, eadl4027 (2024).
43. Liu, T. et al. Thermal photonics with broken symmetries. *eLight* **2**, 25 (2022).
44. Feng, X. et al. Large-area low-cost multiscale-hierarchical metasurfaces for multispectral compatible camouflage of dual-band lasers, infrared and microwave. *Adv. Funct. Mater.* **32**, 2205547 (2022).
45. Hong, S. et al. An adaptive and wearable thermal camouflage device. *Adv. Funct. Mater.* **30**, 1909788 (2020).
46. Xu, Z. H. et al. Chimera metasurface for multiterrain invisibility. *Proc. Natl Acad. Sci.* **121**, e2309096120 (2024).
47. Fang, S. et al. Self-assembled skin-like metamaterials for dual-band camouflage. *Sci. Adv.* **10**, eadl1896 (2024).
48. Wei, H. et al. Tunable VO2 cavity enables multispectral manipulation from visible to microwave frequencies. *Light Sci. Appl.* **13**, 54 (2024).
49. Zhu, H. et al. Multispectral camouflage for infrared, visible, lasers and microwave with radiative cooling. *Nat. Commun.* **12**, 1805 (2021).
50. Qin, B. et al. Whole-infrared-band camouflage with dual-band radiative heat dissipation. *Light Sci. Appl.* **12**, 246 (2023).
51. Xu, J. et al. Broadband directional control of thermal emission. *Science* **372**, 393–397 (2021).
52. Xi, W. et al. Ultrahigh-efficient material informatics inverse design of thermal metamaterials for visible-infrared-compatible camouflage. *Nat. Commun.* **14**, 4694 (2023).
53. Jia, Y. et al. Transparent dynamic infrared emissivity regulators. *Nat. Commun.* **14**, 5087 (2023).
54. Li, M. et al. Manipulating metals for adaptive thermal camouflage. *Sci. Adv.* **6**, eaba3494 (2020).
55. Zhang, Y. et al. Chameleon-inspired tunable multi-layered infrared-modulating system via stretchable liquid metal microdroplets in elastomer film. *Nat. Commun.* **15**, 5395 (2024).
56. Li, L. et al. Ultrathin titanium carbide (MXene) films for high-temperature thermal camouflage. *Adv. Funct. Mater.* **31**, 2101381 (2021).
57. Zhang, L. et al. A thermally robust and optically transparent infrared selective emitter for compatible camouflage. *J. Mater. Chem. C* **9**, 15018–15025 (2021).
58. Kim, Y. et al. Parallel laser printing of a thermal emission pattern in a phase-change thin film cavity for infrared camouflage and security. *Laser Photonics Rev.* **16**, 2100545 (2021).
59. Yu, S. et al. General deep learning framework for emissivity engineering. *Light Sci. Appl.* **12**, 291 (2023).
60. Kim, S. et al. High-performance transparent radiative cooler designed by quantum computing. *ACS Energy Lett.* **7**, 4134–4141 (2022).
61. Micheletti, C. et al. Polymer physics by quantum computing. *Phys. Rev. Lett.* **127**, 080501 (2021).
62. He, M. et al. Deterministic inverse design of Tamm plasmon thermal emitters with multi-resonant control. *Nat. Mater.* **20**, 1663–1669 (2021).
63. MIL-PRE-53134. Ultra-lightweight camouflage net system (ULCANS). *Military Specification of USA*, USA.
64. Wang, Y. et al. Detection and anti-detection with microwave-infrared compatible camouflage using asymmetric composite metasurface. *Adv. Sci.* 2410364 (2024).
65. Kuang, C. et al. Electrically tunable infrared optics enabled by flexible ion-permeable conducting polymer-cellulose paper. *npj Flex. Electron.* **8**, 55 (2024).
66. Siegel, J. et al. Electrostatic steering of thermal emission with active metasurface control of delocalized modes. *Nat. Commun.* **15**, 3376 (2024).
67. Qin, B. et al. Space-to-ground infrared camouflage with radiative heat dissipation. *Light.: Sci. Appl.* **14**, 137 (2025).
68. Zhao, M. et al. High-temperature stealth across multi-infrared and microwave bands with efficient radiative thermal management. *Nano-Micro Lett.* **17**, 199 (2025).
69. Yu, J. et al. Asymmetric directional control of thermal emission. *Adv. Mater.* **35**, 2302478 (2023).
70. Dai, C. et al. Approaching the thermal emissivity limit with ultrathin MXene films. *Optica* **12**, 685–692 (2025).

Acknowledgements

The authors most gratefully acknowledge Dr. Jiabao Sun of Micro-Nano Fabrication Center, Zhejiang University, for his professional and enthusiastic assistance during the EBE experiments. The authors thank Liying Chen from the State Key Laboratory of Extreme Photonics and Instrumentation, Zhejiang University, for her help in the FTIR experiments. The authors thank Miao Huang and colleagues from LUSTER LightTech Co., Ltd for their invaluable assistance with the hyperspectral demonstration. The authors thank Dualix Spectral Imaging Co., Ltd for their invaluable assistance with the hyperspectral demonstration. This work is supported by the National Key Research and Development Program of China (Grant No. 2024YFA1210500 (Q.L.)), National Natural Science Foundation of China (Grant No. U2341225 (Q.L.)), Sichuan Science and Technology Program (Grant No. 2025YFHZ0297 (Q.L.)), the China Postdoctoral Science Foundation (Grant Nos. 2024M762817 and 2025T180236 (H.Z.)), and Postdoctoral Fellowship Program of CPSF (Grant No. GZB20240647 (H.Z.)).

Author contributions

Q.L. conceived the idea and supervised the project together with M.Q. R.Z. performed the calculations and experiments. B.Q. and W.Y. participated in the design and fabrication. M.Z., N.Y., Z.S., and H.M. participated in the multispectral demonstration. R.Z. and Q.L. wrote the initial manuscript. M.Q., H.Z., P.G., L.X., and J.H. reviewed and revised the manuscript. All authors discussed the results and contributed to the final version of the manuscript.

Competing interests

The authors declare no competing interests.

Additional information

Supplementary information The online version contains supplementary material available at https://doi.org/10.1038/s41467-025-63563-3.

Correspondence and requests for materials should be addressed to Qiang Li.

Peer review information *Nature Communications* thanks the anonymous reviewer(s) for their contribution to the peer review of this work. A peer review file is available.

Reprints and permissions information is available at http://www.nature.com/reprints

Publisher's note Springer Nature remains neutral with regard to jurisdictional claims in published maps and institutional affiliations.

Open Access This article is licensed under a Creative Commons Attribution-NonCommercial-NoDerivatives 4.0 International License, which permits any non-commercial use, sharing, distribution and reproduction in any medium or format, as long as you give appropriate credit to the original author(s) and the source, provide a link to the Creative Commons licence, and indicate if you modified the licensed material. You do not have permission under this licence to share adapted material derived from this article or parts of it. The images or other third party material in this article are included in the article's Creative Commons licence, unless indicated otherwise in a credit line to the material. If material is not included in the article's Creative Commons licence and your intended use is not permitted by statutory regulation or exceeds the permitted use, you will need to obtain permission directly from the copyright holder. To view a copy of this licence, visit http://creativecommons.org/licenses/by-nc-nd/4.0/.

© The Author(s) 2025